

Automatic Choroid Vascularity Index Calculation in Optical Coherence Tomography Images Low Contrast Sclerochoroidal Junction Using Deep Learning

Roya Arian

Isfahan University of Medical Sciences

Tahereh Mahmoudi

Tehran University of Medical Sciences and Research Centre of Biomedical Technology and Robotics (RCBTR)

Hamid Riazi-Esfahani

Tehran University of Medical Sciences

Rahele Kafieh (✉ rkafieh@gmail.com)

Newcastle University

Hooshang Faghihi

Tehran University of Medical Sciences

Ahmad Mirshahi

Tehran University of Medical Sciences

Fariba Ghassemi

Tehran University of Medical Sciences

Alireza Khodabande

Tehran University of Medical Sciences

Elias Khalili Pour

Tehran University of Medical Sciences

Research Article

Keywords: Choroidal vascularity index (CVI), optical coherence tomography (OCT), total choroidal area (TCA), luminal area (LA), pachychoroid spectrum

Posted Date: December 20th, 2021

DOI: <https://doi.org/10.21203/rs.3.rs-1150024/v1>

License:   This work is licensed under a Creative Commons Attribution 4.0 International License. [Read Full License](#)

Abstract

Choroidal vascularity index (CVI) is a new biomarker defined for retinal optical coherence tomography (OCT) images for measuring and evaluating the choroidal vascular structure. CVI is the ratio of the choroidal luminal area (LA) to the total choroidal area (TCA). The automatic calculation of this index is important for ophthalmologists but has not yet been explored. In this study, we proposed a fully automated method based on deep learning for calculating CVI in three main steps: 1- segmentation of the choroidal boundary, 2- detection of the choroidal luminal vessels, and 3- computation of the CVI. The proposed method is evaluated in complex situations like the presence of diabetic retinopathy and pachychoroid spectrum. In pachychoroid spectrum, the choroid is thickened, and the boundary between choroid and sclera (sclerochoroidal junction) is blurred, which makes the segmentation more challenging. The proposed method is designed based on the U-Net model, and a new loss function is proposed to overcome the segmentation problems. The vascular LA is then calculated using Niblack's local thresholding method, and the CVI value is finally computed. The experimental results for the segmentation stage with the best-performing model and the proposed loss function were used showed dice coefficients of 0.941 and 0.936 in diabetic retinopathy and pachychoroid spectrum patients, respectively. The unsigned boundary localization errors in the presence of diabetic retinopathy were 0.0020 and 0.0138 pixels for the BM boundary and sclerochoroidal junction, respectively. Similarly, the unsigned errors in the presence of pachychoroid spectrum were 0.0072 and 0.0254 pixels for BM and sclerochoroidal junction. The performance of the proposed method for calculating CVI was evaluated; the Bland-Altman plot indicated acceptable agreement between the values allocated by experts and the proposed method in the presence of diabetic retinopathy and pachychoroid spectrum.

1. Introduction

The choroid is a vascularized tissue located between the retina (as the innermost layer of the eye) and the sclera (as the outermost layer of the eye). It has the highest blood flow of all tissues in the human body. This layer is responsible for supplying blood to the outer parts of the retina and the optic nerve (1). Choroidal changes occur primarily or secondarily in many ocular diseases. The inspection of choroidal changes adjoined with information from the retina leads to better understandings of the pathogenesis of diverse diseases and how to control responses to treatments (2).

Despite the valuable clinical information that has been gained through choroidal thickness (CT), it only represents the overall choroidal structure, providing no distinctions between the stromal and luminal vascular components (2). Recently, the choroidal vascularity index (CVI), defined as the ratio of the choroidal luminal area (LA) to the total choroidal area (TCA), has been employed to evaluate the vascular structure of choroids in different retinal and choroidal disorders (2, 3). Since CVI's introduction, many investigations have measured its effectiveness as a useful method for disease prognostication and tracking progression, with positive findings (1, 4–8).

Optical coherence tomography (OCT) has become a crucial tool in retinal imaging that provides noninvasive, high-resolution cross-sectional images from the retinal layers in vivo. OCT is a preferred imaging technique and is essential for the diagnosis and management of many retinal diseases associated with the choroid. Preliminary OCT imaging devices did not have adequate resolution to demonstrate the choroidal layers, particularly the sclerochoroidal junction as the outermost boundary of the choroid. The main reason was the absorption and scattering of emitted light from the OCT device by the overlying layers, especially in patients with a thick choroid (pachychoroid spectrum) (3, 9). The advent of enhanced depth imaging (EDI)-OCT and swept-source (SS)-OCT facilitated the investigation of choroidal structures like the vascular layers and outer borders of choroid for quantitative evaluation of biomarkers like CT and

CVI (10, 11). However, even with such novel techniques now available, the segmentation of the choroid and sclerochoroidal junction remains challenging.

The exact localization of the sclerochoroidal junction provides useful numerical information, like CVI, that acts as a new OCT-based biomarker and can be employed for measuring and evaluating the choroidal vascular structure in chorioretinal disorders. Manual measurements of CVI are time-consuming, prone to objective error, and require much effort. Thus, manual measurement procedures have raised concerns about their suitability for volumetric analysis (4). Accordingly, the automatic calculation of CVI is introduced as a crucial task including three main steps: 1- segmentation of choroidal layer, 2- detection of choroidal luminal vessels, and 3- computation of the CVI.

Regarding the first task, previous segmentation algorithms for detecting choroidal boundaries relied on standard image processing methods, such as graph theory-based approaches, active contour, and statistical model-based methods (12–15). Graph-based approaches have exhibited better performance than the other methods, but they suffer from a lack of interaction constraints with high processing time (12, 14). Recently, deep learning-based architectures have been successfully applied in the field of biomedical image segmentation of the retina, liver, brain, pancreas, heart, and other structures (16-19).

In work related to the segmentation of the choroidal layer, patch-based approaches were presented using CNN for the segmentation of RPE and choroidoscleral interface (CSI) boundaries (20–22). In other studies, a combination of deep learning and graph cut algorithms were used for choroidal boundary segmentation (23, 24). Mao et al. suggested skip connection attention (SCA) block integrated into the U-shape architectures, such as U-Net and context encoder network (CE-Net), for automated choroid layer segmentation (25). They showed that SCA embedded into CE-Net performs better for choroid layer segmentation. Xu et al. applied an automated method for PED segmentation in polypoidal choroidal vasculopathy using a deep neural network (26). Zheng et al. carried out choroid layer segmentation to obtain several evaluation parameters in swept-source OCT images from a healthy population. Residual U-Net was used to segment the choroidal boundaries (27).

Table 1 provides a better comparison of the previous methods by summarizing the recent deep learning works for choroid layer segmentation and comparing them from different aspects, such as dataset, device, proposed method, loss function, metrics, and results.

Table 1
Summary of the previous studies in choroid layer segmentation using deep learning approaches

Paper	Data	Device name	Method	Loss Function	Metrics	Result	
Mao et.al (25)	20 normal human subjects	Topcon DRI-OCT-1	SCA-CENet	Not Reported	Sensitivity	0.918	
					F1-Score	0.952	
					Dice-Coefficient	0.951	
					IoU	0.909	
					MAE (BM)	1.945	
					MAE (SCI)	8.946	
Kugelman et.al (20)	99 Children,594 B-scans	SD-OCT	Patch base classification	Tverksy loss	ME(in pixel)	ILM	0.01
						BM	0.03
						CSI	-0.02
			CNN-RNN		MAE (in pixel)	ILM	0.45
						BM	0.46
						CSI	3.22
Masood et.al (21)	11 Normal, 4ShortSightedness, 4 Glaucoma, 3 DME	swept-source OCT	Morphological processing and CNN	Cross entropy loss	Signed error (in pixel)	BM	0.43 ± 1.01
						Choroid	2.8 ± 1.50
						Unsigned error (in pixel)	BM
Choroid	2.89 ± 1.05						
Sui et.al (23)	912 B-scans (618 scans normal, 294 macular edema	EDI-OCT	Graph-based and CNN	MSE	Absolute error(in pixel)	BM	4.6±4.8
						CSI	11.4±11.0
Xu et.al (26)	50 PCV patients (1800 B-scans)	SD-OCT	Dual-stage DNN	Log-loss	Unsigned error (in μ m)	BM	5.71 ± 3.53
Tsuji et al. (24)	43 eyes from 34 healthy individual	SS-OCT	SegNet and Graph cut	Not reported	Dice-Coefficient		0.909±0.505
He et al. (22)	146 OCT images	SD-OCT	Patch-based CNN Classifier	Focal loss	Dice-Coefficient		0.904±0.055
Zheng et al. (27)	450 images from 12 healthy individual	SS-OCT	residual U-Net	Not reported	Failure ratio less than 0.02mm		68.84%

As discussed above, the second task for automatic calculation of CVI is the detection of choroidal luminal vessels. Histopathological assessment is the gold standard for investigating the choroidal vascular area. However, it is not a practical clinical tool since it is dependent on autopsy or biopsy samples and due to post-fixation shrinkage and

distortion resulting in the lack of repeatability and reliability. On the other hand, it is almost impossible to label the images manually due to the complex structure and the substantial amount of time required.

After comparing different image segmentation techniques, Agrawal et al., the pioneers of CVI measurement, adopted Niblack's auto local threshold technique in many studies of CVI while considering different healthy and pathologic conditions. This is because it considers the mean and standard deviation of all the pixels in the region of interest (4).

Vupparanbina et al. (28) pioneered the transition to automated CVI analysis. Recently, Betzler et al. developed an automated platform for measuring CVI (www.cvigrd.org). Their automated algorithm was not officially released at the time of writing this manuscript. It is based on multistep sequential image processing algorithms and allows for manual ROI modification to suit scans of various widths (4,29).

The proposed method is designed to fulfill the three steps mentioned above with fully automated algorithms. For this purpose, we adopted Niblack thresholding to develop software that is clinically acceptable and can be used by clinicians with comparable results to most well-known works in this area.

- A fully automated method with freely available code is proposed for the first time to calculate the CVI value in diabetic retinopathy and pachychoroid spectrum using deep learning methods.
- The proposed modified U-Net can segment the choroid and BM boundaries in challenging cases like low contrast images with thickened choroidal areas.
- The proposed loss function (a weighted combination of dice loss (DL), weighted categorical cross entropy (WCCE), and Tversky loss) is shown to be able to overcome the very imbalanced data (small foreground vs. big background).

The remainder of this paper is organized as follows: Section 2 presents the proposed method in detail, Section 3 describes experimental results, and Section 4 discusses the results. The source code of this method is publicly available at <https://github.com/TaherehMahmoudi/OCT-CVI-DeepLearning>.

2. Materials And Methods

2.1. OCT data and manual annotation

The data set used in this study was collected in Farabi Hospital, Tehran University of Medical Sciences, Tehran, Iran. EDI-OCT images were obtained using the RTVue XR 100 Avanti instrument (Optovue, Inc., Fremont, CA, USA). Patients with diabetic retinopathy were positioned appropriately, and equally spaced high-resolution EDI-OCT B-scans at 8 mm * 12 mm long raster patterns were captured. In patients with pachychoroid spectrum, the image acquisition protocol was based on EDI-OCT HD line 8 mm * 12 mm long scans. In a retrospective study, 439 Raster OCT B-scans from 112 patients with diabetic retinopathy and 98 EDI-HD OCT B-scans from 44 patients with pachychoroid spectrum were selected for training/validating and testing the model. The study was approved by the Tehran University of Medical Sciences Institutional Review Board (IRB) (IR.TUMS.FARABIH.REC.1399.017) and adheres to tenets of the Declaration of Helsinki. Written informed consent was obtained from all participants. The subjects' demographics and clinical characteristics are reported in Table 2.

For manual demarcation of choroidal boundaries as ground truth, raw OCT images were imported using ImageJ software (<http://imagej.nih.gov/ij/>), which is provided in the public domain by the National Institutes of Health, Bethesda, MD, USA. Choroidal borders of all images were delineated by the polygonal selection tool in the software toolbar. RPE-Bruchs membrane complex (BM) and the sclerochoroidal border were selected as the upper and lower

margins of the choroid, respectively. The edge of the optic nerve head and the most temporal border of the image were selected as the nasal and temporal margins of the choroidal area. All manual segmentations were conducted by a skilled grader (EKH) and verified by another independent grader (HRE). In case of any disputes, the outlines are segmented by consensus.

Table 2
Demographics and clinical characteristics of the patients

Data	Pachychoroid spectrum	Diabetic Retinopathy
No. of patients	44	112
No. of B-scan Images	98	439
Mean Age (mean±SD)	50.6±11.2 (range:29-74 years)	61±8 (range:47-78years)
Gender	37(84.1%) male	59(52.6%) male
Best Corrected Visual Acuity (BCVA) (mean±SD)	0.50±0.38	0.57±0.25
Subfoveal choroidal Thickness (range in μm)	(265-510 μm)	(135-370 μm)

2.2. Manual calculation of CVI

According to the method introduced by Sonoda et al. (30), the total choroidal area was manually selected from the optic nerve to the temporal side of the image. The selected area was added as a region of interest (ROI) with the ROI manager tool. CVI was calculated in selected images from both diabetic and pachychoroid spectrum groups by randomly selecting three sample choroidal vessels with lumens larger than 100 μm by the oval selection tool in the toolbar. The average reflectivity of these areas was determined by the software. The average brightness was set as the minimum value to minimize the noise in the OCT image.

Then, the image was converted to 8 bits and adjusted by the auto local threshold of Niblack. The binarized image was reconverted into an RGB image, and the luminal area was determined using the color threshold tool. The light pixels were defined as the choroidal stroma or interstitial area, and the dark pixels were defined as the luminal area. The total choroidal area (TCA), luminal area (LA), and stromal area (SA) were automatically calculated (30).

Herein, we refer to the ratio of LA to TCA as the choroidal vascularity index (CVI). The CVI is calculated separately for each image.

2.3. Fully automated Calculation of CVI Using Deep Learning

Fully automated calculations of CVI include three main steps: segmenting the choroidal layer, detecting the choroidal luminal vessels, and computing the CVI. These steps are elaborated in the following sections.

2.3.1. Automatic segmentation of the choroidal layer

In the proposed method, manual segmentation of the choroidal area was utilized to construct the ground truth masks. The choroid area is of interest in this work; using a simple approach, we needed to perform two-class segmentation to divide the image into the choroid area (foreground) and the rest of the image (background), as this is the most prevalent technique used in similar works. However, we found that the backgrounds of the upper and lower choroid areas have different textures because they refer to different anatomical structures. Accordingly, we selected the three-class approach to consider the intrinsic differences of the ocular structures. The second approach yielded better

results after being trained with similar data, and we used it as our final segmentation approach to be used in the next stages and CVI calculation.

All original images (figure 1-a) were cropped to set the most nasal side of the macula on the margins of the optic disc (figure 1-a1), thus eliminating the unwanted areas of the image. Two distinct models (two-class and three-class approaches) were trained separately on the cropped images.

- In the two-class segmentation approach, all pixels of the choroidal area (target class) were replaced by white pixels (Figure 1-b2).
- In the three-class segmentation approach, the cropped image was divided into three regions (Figure 1-c2).

The block diagram of the proposed approach is depicted in Figure 1.

Figure 1. Block diagram of the proposed method. The unwanted area of the original image is cropped in (a1). Two approaches)2-class (b1,2) and 3-class (c1,2)) are used for segmentation of the choroid area using U-net (d). After denoising of the obtained image (e), vascular LA detection is carried out using Niblack's auto local threshold (f). CVI is finally calculated using the ratio of the LA to the TCA.

2.3.1.1. Network Architectures

A U-Net network with a connectivity-promoting regularization loss function is used both for two- and three-class segmentation approaches (Figure 2). U-Net, originally proposed by Ronneberger et al., is one of the most popular segmentation models in medical imaging based on encoder-decoder architecture and the use of skip connections (31). The number of filters in the proposed method started at 32 and continued for five stages with a learning rate of 0.0000001 and an Adam optimizer.

2.3.1.2. Modified Loss Function

One of the main issues in the segmentation of a relatively thin layer from a whole image is handling the unbalanced data. Standard losses such as cross-entropy loss and dice loss usually fail on such occasions, and some new substitutes have already been introduced to solve the problem.

For instance, Tversky loss is introduced as an alternative to dice coefficient, which treats false negative (FNs) and false positive (FPs) equally, resulting in higher recall and lower precision. Tversky loss was proposed (32) to overcome this issue by weighing FNs more heavily than FPs for imbalanced data.

On the other hand, WCCE is introduced to replace the most famous loss function in classification problems, categorical cross entropy (CCE). WCCE weighs the foreground more heavily than the background (choroid area vs. the whole image) and can be useful for imbalanced data. To design the weights of WCCE in ($j = 3$) class segmentation, we used the following equation:

$$w_j = \frac{1 - f_{w_j}^\beta}{1 - \beta} \quad (1)$$

where w_j is a weight vector in WCCE, f_j is the ratio indicating the area corresponding to class j compared to the whole area, and β is a hyperparameter ($\beta \in [0,1)$) chosen empirically as 0.8 in this study.

Finally, considering that the desired segmented region (choroid area) has an interconnected structure and that the anatomical background does not yield disjoint sections, total variation (TV) loss is expected to model these characteristics.

In order to consider the mentioned loss functions, we investigated the results of using each individual loss function and their combination. Four different loss functions are examined:

Loss Function #1: dice loss

Loss Function #2: dice loss + Weighted Categorical Cross Entropy (WCCE) (33)

Loss Function #3: dice loss + WCCE+ Total Variation (TV)

Loss Function #4: dice loss + WCCE+ Tversky

2.3.1.3. A train/test split and metrics of the segmentation model

It is crucial to split the data at the patient level (not the bscans-level) to avoid any leakage between test and train or any correlation between the images in test and train data. For this purpose, we divided the datasets deliberately to avoid any such leakage. Regarding the images from diabetic retinopathy, from 112 patients, 25 patients are randomly selected as test data, and the rest are used as train/validation data. Regarding the pachychoroid cases from 44 patients, 10 patients (20 images) are selected as test data, and the rest are employed in the train/validation data stage.

For evaluating the accuracy of the segmentation, the predicted masks of the choroid layer are compared with manual masks, and the dice similarity coefficient (DSC) is calculated based on the following equation:

$$DSC = \frac{2(A \cap B)}{A + B}$$

2

where A and B are the predicted and ground truth masks, respectively. The average DSC on all B-scans of the test dataset is reported in Section 3. Furthermore, the mean absolute error between predicted boundaries and the manually annotated boundaries are calculated and reported.

The following steps were performed to measure CVI in pachychoroid spectrum and diabetic retinopathy subjects:

- Calculation of the BM boundary and sclerochoroidal junction based on the choroidal layer mask from U-Net architecture, as elaborated above.
- Noise reduction using non-local means algorithm with a deciding filter strength of 10 (34).
- Vascular LA detection using Niblack's auto local threshold method using Python software. The selected parameters for Niblack's method are summarized in Table 3 to make the provided code reproducible. The parameters are empirically adjusted to resemble gold standard values as much as possible in the training dataset.
- Calculation of CVI using

$$CVI = \frac{vascularluminalarea}{totalchoroidalarea}$$

Table 3
Parameters used for Niblack's algorithm in two datasets.

Parameter of Niblack's algorithm	Diabetic Retinopathy images	Pachychoroid spectrum images
Window size	15	13
K	0.001	0.01
Threshold coefficient	1.03	1.02

3. Results

The software environment used in this study consists of the Keras platform backend in python 3.7 with NVIDIA GeForce GTX 1080Ti GPU. The performances of different proposed segmentation methods were compared considering the values of signed error (S_E) and unsigned error (U_E) for localization of the BM boundary and sclerochoroidal junction (reported in pixels). Furthermore, DSC for each method is reported and compared. In addition, the calculation of CVI values was evaluated based on the Bland Altman plot among manual and automated measurements.

3.1. Choroidal boundary segmentation in pachychoroid spectrum dataset

We compared the performances of different loss functions for two-class and three-class segmentation approaches in the localization of choroidal boundary in pachychoroid spectrum patients. The segmentation results of each loss function (on two examples) are demonstrated in Figure 3. Manually annotated boundaries for each image are shown in red, while predicted ones are depicted in blue.

For further validation purposes, the mean signed and unsigned boundary positioning errors for each layer are reported in Table 4. These errors are normalized by dividing them by the input image size of the model. The experimental results with different batch sizes, input image sizes, and test-train split ratios are reported in the appendix.

Table 4
Mean signed and unsigned error (S_E and U_E) for different loss functions in two- and three-class segmentation of the pachychoroid spectrum dataset (in pixels).

Unit	Loss Function	Two-class segmentation				Three-class segmentation			
		BM Boundary		Choroid Boundary		BM Boundary		Choroid Boundary	
		U_E	S_E	U_E	S_E	U_E	S_E	U_E	S_E
Pixel	Loss#1	0.0149	-0.0032	0.0319	-0.0126	0.0074	-0.0055	0.0305	0.0056
	Loss#2	0.0113	-0.0106	0.0309	0.0075	0.0073	-0.0066	0.0260	0.0042
	Loss#3	0.0130	0.0013	0.0291	0.0039	0.0075	-0.0037	0.0261	0.0051
	Loss#4	0.0101	-0.0085	0.0281	-0.0019	0.0072	-0.0048	0.0254	-0.0085

3.2. Choroidal boundary segmentation in the diabetic retinopathy dataset

Similar to the pachychoroid spectrum dataset, the segmentation results are shown in Figure 4, and the boundary positioning errors are reported in Table 5. The experimental results with different batch sizes, input image sizes, and test-train split ratios are again reported in the appendix.

Table 5

Mean signed and unsigned error (S_E and U_E) for different loss functions in two- and three-class segmentation of the diabetic retinopathy (in pixels).

Unit	Loss Function	Two-class segmentation				Three-class segmentation			
		BM boundary		Sclerochoroidal boundary		BM boundary		Sclerochoroidal boundary	
		U_E	S_E	U_E	S_E	U_E	S_E	U_E	S_E
Pixel	Loss#1	0.0201	0.0045	0.0301	0.0129	0.0033	-0.0029	0.0143	-0.0022
	Loss#2	0.0150	0.0023	0.0248	0.0097	0.0021	-0.0010	0.0139	0.0003
	Loss#3	0.0152	0.0032	0.0251	0.0110	0.0021	-0.0007	0.0148	-0.0049
	Loss#4	0.0141	0.0011	0.0209	-0.0006	0.0020	0.0001	0.0138	0.0001

In addition, the DSC for each proposed combination of loss functions is shown in Figure 5 to provide a visual comparison between different loss functions. The results indicate that the best performance is exhibited by the three-class segmentation combination of the best-chosen loss function (DL, WCCE, and Tversky losses). The sample results using the best-selected model are demonstrated in Figure 6 for diabetic retinopathy and pachychoroid spectrum data.

Vascular LA segmentation CVI measurement

The results of vascular LA segmentation using Niblack's method are shown in Figure 7. Automated and manual CVI for pachychoroid spectrum and diabetic retinopathy were measured, and the Bland-Altman limits of agreement between manual and automated measurements were calculated for pachychoroid spectrum and diabetic retinopathy data. Bland-Altman plots were used to graphically represent the agreement between manual and automated methods in CVI measurements, as shown in Figure 8. Limits of agreement between the automated and manual methods to measure CVI ranged from -0.168 to 0.120 to and -0.080 to 0.095 to for pachychoroid spectrum and diabetic retinopathy data, respectively.

Discussion

The recently introduced metric, CVI, was developed in response to the need for choroidal vasculature assessments that are more reliable and precise than previous measures such as CT and choroidal vessel diameter, which have limitations. CVI displayed less changeability than CT and was influenced by fewer physiologic elements in previous studies, showing that it is a generally stable biomarker for studying choroidal modifications (4-6).

The need for automatic calculations of CVI is undeniable in the presence of a high number of OCT scans; also, there is no fully automatic method with freely available code to address this issue. In the current study, a U-Net architecture was used to segment the RPE boundary and sclerochoroidal junction. A tailored set of loss functions with a combination of four classic losses (such as dice loss coefficient (DL), weighted categorical cross-entropy (WCCE), total variation (TV), and Tversky) are examined to fulfill the need for managing the imbalanced data in segmentation of small regions in an image.

Subsequently, the desired task is inspected using two-class and three-class segmentation approaches. At first, we carried out a two-class approach. One class was the choroid area, and the rest of the image was the other class. As the upper and lower choroid areas have different textures, we used a three-class approach as the final approach. Experimental results showed that the three-class approach performed better at segmenting the choroid area, and we used this network for final segmentation to obtain the CVI. Experimental results with three-class segmentation using combined loss (dice, WCCE, and Tversky) showed dice coefficients of 0.941 and 0.936 in diabetic retinopathy and pachychoroid spectrum patients, respectively (Figure 5).

In the presence of diabetic retinopathy, the unsigned boundary localization errors are 0.0020 and 0.0138 pixels for the BM boundary and sclerochoroidal junction, respectively. However, in the presence of the pachychoroid spectrum, the unsigned errors are 0.0072 and 0.0254 pixels for BM and sclerochoroidal junction, respectively (Tables 4 and 5).

Then, Niblack's auto local threshold is adopted to calculate the vascular LA in accordance with clinically approved publications. The CVI value is then calculated based on this stage, and the Bland-Altman plot indicated an acceptable agreement between manually allocated values and the proposed method for CVI calculation.

The results of our study showed that the designed deep learning algorithm can detect RPE with higher accuracy than sclerochoroidal junction due to the higher intensity of RPE signal in OCT images compared to the sclerochoroidal junction.

Previous studies were limited to normal OCT scans, and the challenge of segmenting blurred boundaries is achieved in this work. There is just one available code called OCT-tool (35) that can be used to segment choroidal layer. Using this code, BM boundary of each test data is automatically detected however the choroid boundary is detected manually by adding some control points. It takes a long time to add enough control points and fit the choroid layer. But in the current study this layer is automatically detected with high accuracy which is greatly time consuming.

Due to the uncertainty of the sclerochoroidal junction, choroidal segmentation is difficult in patients with thick choroidal, such as patients with pachychoroid spectrum. Therefore, in this study, in addition to diabetic patients, a group of patients with pachychoroid spectrum was included. Moreover, we considered ROI extended from the optic nerve to the temporal side of the image to get a more precise estimate of CVI. While Agrawal et al. (6) demonstrated that subfoveal CVI can accurately reflect the CVI of the entire macular area in healthy individuals, this assertion does not hold in pachychoroid disease or ethnicities with the thicker choroid.

The limitations of our study include the following. This study was performed on just a small number of OCT scans and included only two disease entities: diabetic retinopathy and pachychoroid spectrum. At best, the accuracy of our algorithm is in the range of 10 microns around the sclerochoroidal junction in both groups of patients with diabetic retinopathy and pachychoroid spectrum. Although this accuracy seems acceptable in patients in the current study, it may not be satisfactory in patients with a very thin choroid, such as patients with age-related macular degeneration. The same is true for patients with very thick choroidal structures, such as patients with infiltrative choroidal disease (e.g., Vogt-Koyanagi-Harada).

Moreover, the OCT scans used in the current study were captured by an RTVue XR 100 Avanti instrument. However, the results of a previous study by Agrawal et al. showed that CVI measurement was not affected by the device used (SD-OCT vs. swept-source) (36). However, to generalize the results of deep learning algorithms to other diseases, these algorithms should be evaluated by diverse devices and in different diseases.

In conclusion, our limited experience showed that a deep learning-based algorithm for the automatic calculation of CVI in OCT images of patients suffering from diabetic retinopathy and pachychoroid spectrum can yield good performance in this regard. Larger-scale studies on different retinochoroidal diseases with more OCT scans captured with different devices can improve automated measurements of CVI, which is a useful biomarker for diagnosis and prognostication.

Declarations

Competing interest statement

The authors declare no competing interests.

Data and code Availability

The data and code are publicly available at <https://github.com/TaherehMahmoudi/OCT-CVI-DeepLearning>.

Acknowledgments

This work was supported in part by the Vice-Chancellery for Research and Technology of Isfahan University of Medical Sciences under Grant 240046 and by the National Institute for Medical Research Development under Grant 964582.

References

1. Nickla DL, Wallman J. The multifunctional choroid. *Prog Retin Eye Res* [Internet]. 2010;29(2):144–68. Available from: <http://dx.doi.org/10.1016/j.preteyeres.2009.12.002>
2. Tan K-A, Gupta P, Agarwal A, Chhablani J, Cheng C-Y, Keane PA, et al. State of science: Choroidal thickness and systemic health. *Surv Ophthalmol* [Internet]. 2016;61(5):566–81. Available from: <http://dx.doi.org/10.1016/j.survophthal.2016.02.007>
3. Singh SR, Vupparaboina KK, Goud A, Dansingani KK, Chhablani J. Choroidal imaging biomarkers. *Surv Ophthalmol* [Internet]. 2019;64(3):312–33. Available from: <http://dx.doi.org/10.1016/j.survophthal.2018.11.002>
4. Agrawal R, Ding J, Sen P, Rousselot A, Chan A, Nivison-Smith L, et al. Exploring choroidal angioarchitecture in health and disease using choroidal vascularity index. *Prog Retin Eye Res* [Internet]. 2020;77:100829. Available from: <http://dx.doi.org/10.1016/j.preteyeres.2020.100829>
5. Agrawal R, Salman M, Tan K-A, Karampelas M, Sim DA, Keane PA, et al. Choroidal Vascularity Index (CVI) - A Novel Optical Coherence Tomography Parameter for Monitoring Patients with Panuveitis? *PLoS One* [Internet]. 2016;11(1):e0146344. Available from: <http://dx.doi.org/10.1371/journal.pone.0146344>
6. Agrawal R, Gupta P, Tan K-A, Cheung CMG, Wong T-Y, Cheng C-Y. Choroidal vascularity index as a measure of vascular status of the choroid: Measurements in healthy eyes from a population-based study. *Sci Rep* [Internet]. 2016;6(1). Available from: <http://dx.doi.org/10.1038/srep21090>
7. Ruiz-Medrano J, Ruiz-Moreno JM, Goud A, Vupparaboina KK, Jana S, Chhablani J. AGE-RELATED CHANGES IN CHOROIDAL VASCULAR DENSITY OF HEALTHY SUBJECTS BASED ON IMAGE BINARIZATION OF SWEEP-SOURCE OPTICAL COHERENCE TOMOGRAPHY. *Retina* [Internet]. 2018;38(3):508–15. Available from: <http://dx.doi.org/10.1097/iae.0000000000001571>
8. Agrawal R, Chhablani J, Tan K-A, Shah S, Sarvaiya C, Banker A. CHOROIDAL VASCULARITY INDEX IN CENTRAL SEROUS CHORIORETINOPATHY. *Retina* [Internet]. 2016;36(9):1646–51. Available from:

<http://dx.doi.org/10.1097/iae.0000000000001040>

9. Sezer T, Altınışık M, Koytak İA, Özdemir MH. The choroid and optical coherence tomography [Internet]. Vol. 46, Turk Oftalmoloji Dergisi. Galenos Yayınevi; 2016. p. 30–7. Available from: <http://dx.doi.org/10.4274/tjo.10693>
10. Wei X, Ting DSW, Ng WY, Khandelwal N, Agrawal R, Cheung CMG. Choroidal vascularity index - A novel optical coherence tomography based parameter in patients with exudative age-related macular degeneration. *Retina*. 2016;0.
11. Chhablani J, Barteselli G. Clinical applications of choroidal imaging technologies. *Indian J Ophthalmol* [Internet]. 2015;63(5):384. Available from: <http://dx.doi.org/10.4103/0301-4738.159861>
12. Danesh H, Kafieh R, Rabbani H, Hajizadeh F. Segmentation of Choroidal Boundary in Enhanced Depth Imaging OCTs Using a Multiresolution Texture Based Modeling in Graph Cuts. *Comput Math Methods Med* [Internet]. 2014;2014:1–9. Available from: <http://dx.doi.org/10.1155/2014/479268>
13. Li K, Wu X, Chen DZ, Sonka M. Optimal Surface Segmentation in Volumetric Images-A Graph-Theoretic Approach. *IEEE Trans Pattern Anal Mach Intell* [Internet]. 2006;28(1):119–34. Available from: <http://dx.doi.org/10.1109/tpami.2006.19>
14. Salafian B, Kafieh R, Rashno A, Pourazizi M, Sadri S. Automatic segmentation of choroid layer in edi oct images using graph theory in neutrosophic space. *arXiv preprint arXiv:181201989*. 2018.
15. Yazdanpanah A, Hamarneh G, Smith B, Sarunic M, editors. Intra-retinal layer segmentation in optical coherence tomography using an active contour approach. *International Conference on Medical Image Computing and Computer-Assisted Intervention*; 2009: Springer.
16. Haque IRI, Neubert J. Deep learning approaches to biomedical image segmentation. *Informatics in Medicine Unlocked*. 2020;18:100297.
17. Mahmoudi T, Kouzahkanan ZM, Radmard AR, Kafieh R, Salehnia A, Davarpanah AH, Arabalibeik H, Ahmadian A. Segmentation of Pancreatic Ductal Adenocarcinoma (PDAC) and Surrounding Vessels in CT Images Using Deep Convolutional Neural Networks and Texture Descriptors. *arXiv preprint arXiv. doi: 10.21203/rs.3.rs-627504/v1*.
18. Pasyar P, Mahmoudi T, Kouzehkanan S-ZM, Ahmadian A, Arabalibeik H, Soltanian N, et al. Hybrid classification of diffuse liver diseases in ultrasound images using deep convolutional neural networks. *Informatics in Medicine Unlocked*. 2021;22:100496.
19. Sobhanian Z, Danesh H, Kafieh R, Determination of foveal avascular zone parameters using a new location-aware deep-learning method. *Proceedings Volume 11843, Applications of Machine Learning 2021; 1184311 (2021)* <https://doi.org/10.1117/12.2594152>.
20. Kugelmann J, Alonso-Caneiro D, Read SA, Hamwood J, Vincent SJ, Chen FK, et al. Automatic choroidal segmentation in OCT images using supervised deep learning methods. *Scientific reports*. 2019;9(1):1-13.
21. Masood S, Fang R, Li P, Li H, Sheng B, Mathavan A, et al. Automatic choroid layer segmentation from optical coherence tomography images using deep learning. *Scientific reports*. 2019;9(1):1-18.
22. He F, Chun RKM, Qiu Z, Yu S, Shi Y, To CH, et al. Choroid Segmentation of Retinal OCT Images Based on CNN Classifier and I2 - Lq Fitter. *Comput Math Methods Med*. 2021;2021.
23. Sui X, Zheng Y, Wei B, Bi H, Wu J, Pan X, et al. Choroid segmentation from optical coherence tomography with graph-edge weights learned from deep convolutional neural networks. *Neurocomputing*. 2017;237:332-41.
24. Tsuji S, Sekiryu T, Sugano Y, Ojima A, Kasai A, Okamoto M, et al. Semantic Segmentation of the Choroid in Swept Source Optical Coherence Tomography Images for Volumetrics. *Sci Rep*. (2020)

25. Mao X, Zhao Y, Chen B, Ma Y, Gu Z, Gu S, et al., editors. Deep Learning with Skip Connection Attention for Choroid Layer Segmentation in OCT Images. 2020 42nd Annual International Conference of the IEEE Engineering in Medicine & Biology Society (EMBC); 2020: IEEE.
26. Xu Y, Yan K, Kim J, Wang X, Li C, Su L, et al. Dual-stage deep learning framework for pigment epithelium detachment segmentation in polypoidal choroidal vasculopathy. *Biomedical optics express*. 2017;8(9):4061-76.
27. Zheng G, Jiang Y, Shi C, Miao H, Yu X, Wang Y, et al. Deep learning algorithms to segment and quantify the choroidal thickness and vasculature in swept-source optical coherence tomography images. *J Innov Opt Health Sci*. 2021;14(1).
28. Vupparaboina KK, Dansingani KK, Goud A, Rasheed MA, Jawed F, Jana S, et al. Quantitative shadow compensated optical coherence tomography of choroidal vasculature. *Scientific reports*. 2018;8(1):1-9.
29. Betzler BK, Ding J, Wei X, Lee JM, Grewal DS, Fekrat S, et al. Choroidal vascularity index: a step towards software as a medical device. *British Journal of Ophthalmology*. 2021.
30. Sonoda S, Sakamoto T, Yamashita T, Uchino E, Kawano H, Yoshihara N, et al. Luminal and stromal areas of choroid determined by binarization method of optical coherence tomographic images. *American journal of ophthalmology*. 2015;159(6):1123-31. e1.
31. Ronneberger O, Fischer P, Brox T, editors. U-net: Convolutional networks for biomedical image segmentation. *International Conference on Medical image computing and computer-assisted intervention*; 2015: Springer.
32. Salehi SSM, Erdogmus D, Gholipour A. Tversky loss function for image segmentation using 3D fully convolutional deep networks. *International Workshop on Machine Learning in Medical Imaging*. 2017; PP 379-387.
33. Phan TH, Yamamoto K. Resolving class imbalance in object detection with weighted cross entropy losses. *arXiv preprint arXiv:200601413*. 2020.
34. Buades A, Coll B, Morel J-M. Non-local means denoising. *Image Processing On Line*. 2011;1:208-12.
35. Stokes S. <https://github.com/sarastokes/OCT-tools>. (2019)
36. Agrawal R, Seen S, Vaishnavi S, Vupparaboina KK, Goud A, Rasheed MA, et al. Choroidal vascularity index using swept-source and spectral-domain optical coherence tomography: a comparative study. *Ophthalmic Surgery, Lasers and Imaging Retina*. 2019;50(2): e26-e32.

Figures

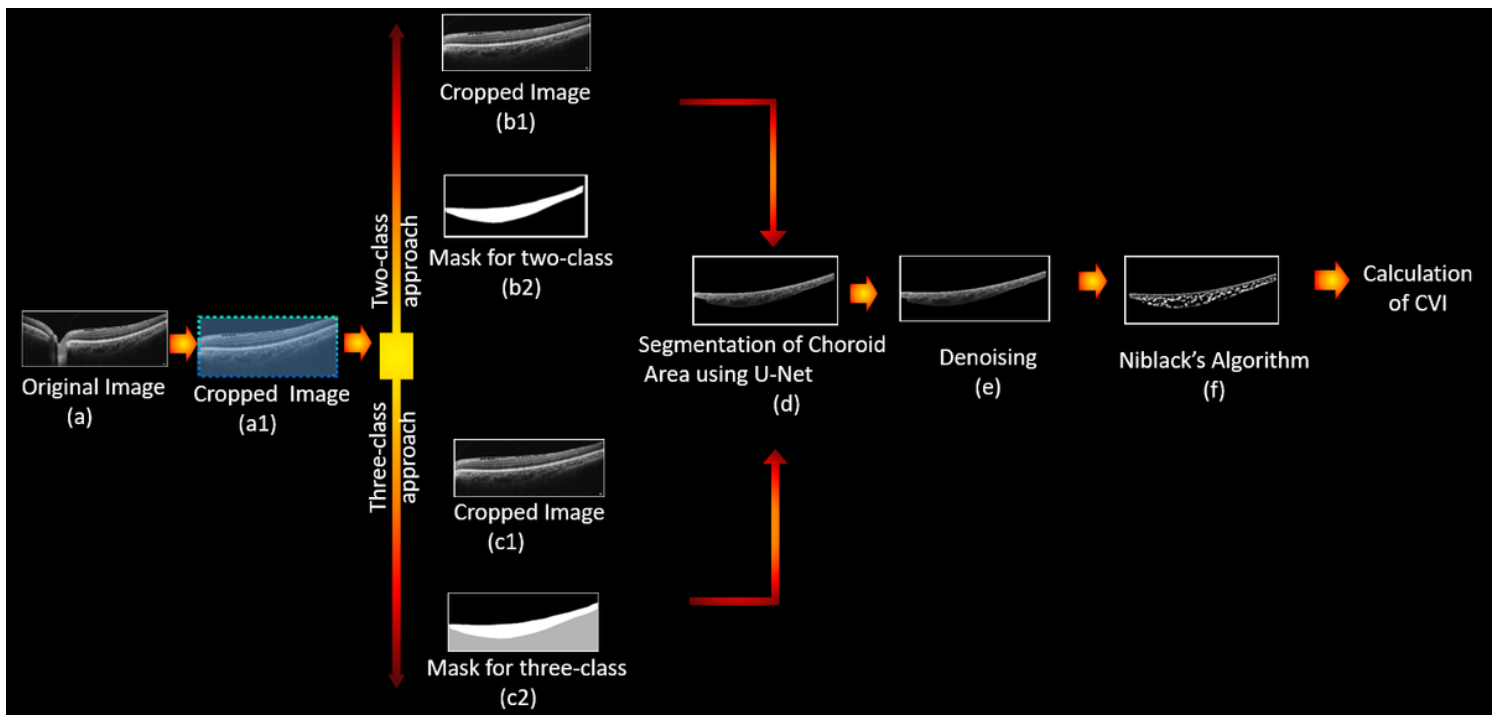


Figure 1

Block diagram of the proposed method. The unwanted area of the original image is cropped in (a1). Two approaches (2-class (b1,2) and 3-class (c1,2)) are used for segmentation of the choroid area using U-net (d). After denoising of the obtained image (e), vascular LA detection is carried out using Niblack's auto local threshold (f). CVI is finally calculated using the ratio of the LA to the TCA.

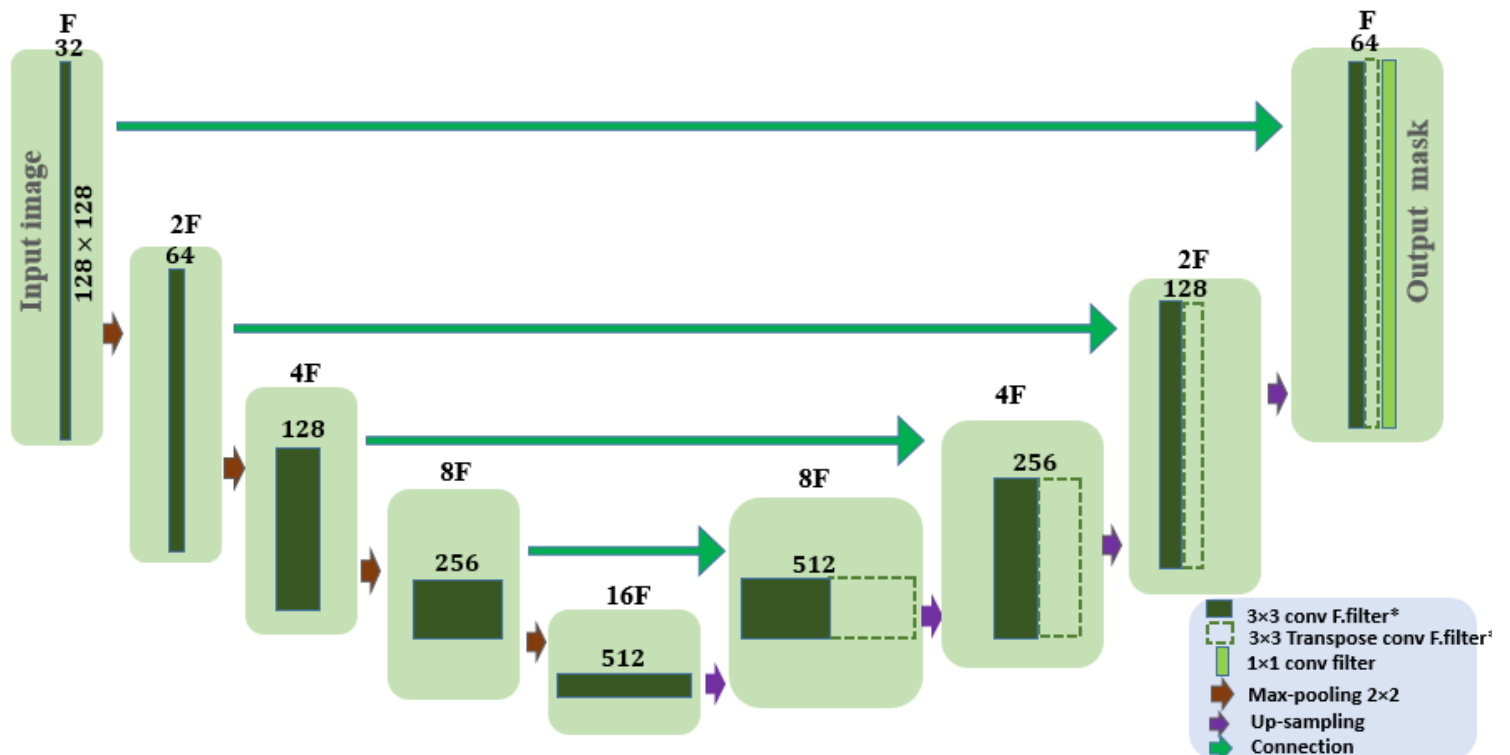


Figure 2

Architecture of the proposed U-Net model

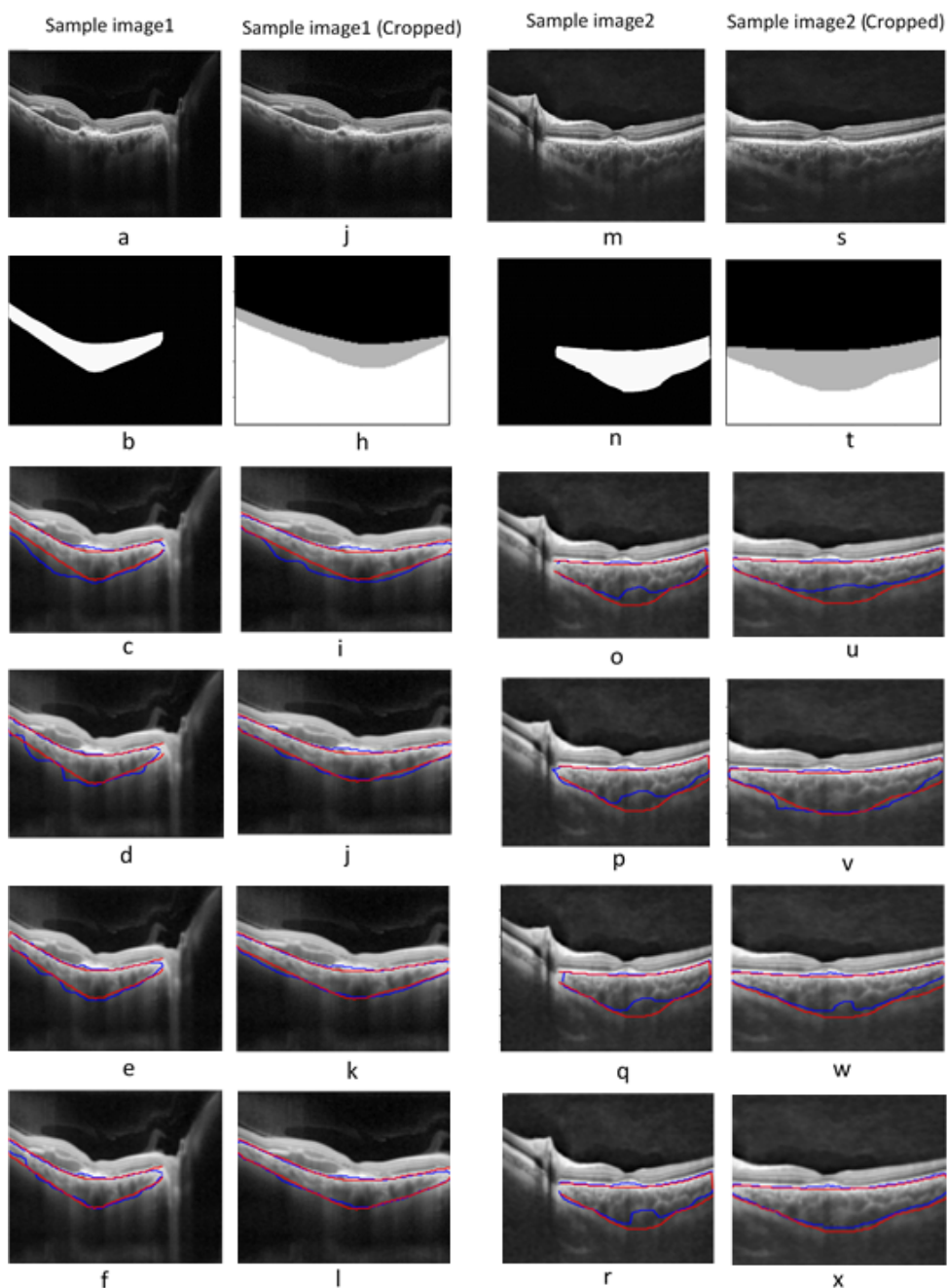


Figure 3

Segmentation results of the two example images in pachychoroid spectrum class. (a) Original pachychoroid spectrum **sample 1**, (b) 2-class ground truth. Real and predicted boundaries of two-class using loss function using (c) DL, (d) DL +WCCE, (e) DL +WCCE + TV, (f) DL +WCCE + Tversky. (g) **Cropped original pachychoroid spectrum sample 1**, (h) 3-class ground truth. Real and predicted boundaries of three-class using loss function: (i) DL, (j) DL +WCCE, (k) DL +WCCE + TV, (l) DL +WCCE + Tversky, (m). Original pachychoroid spectrum **sample 2**, (n) 2-class ground truth. Real and predicted boundaries of two-class, using loss function: (o) DL, (p) DL +WCCE, (q) DL +WCCE + TV, (r) DL +WCCE +

Tversky, (s) **Cropped original pachychoroid spectrum sample 2**, (t) 3-class ground truth, real and predicted boundaries of three-class using loss function: (u) DL, (v) DL +WCCE, (w) DL +WCCE + TV, (x) DL +WCCE + Tversky. Manually annotated boundaries for each image are shown in red where predicted ones are shown in blue.

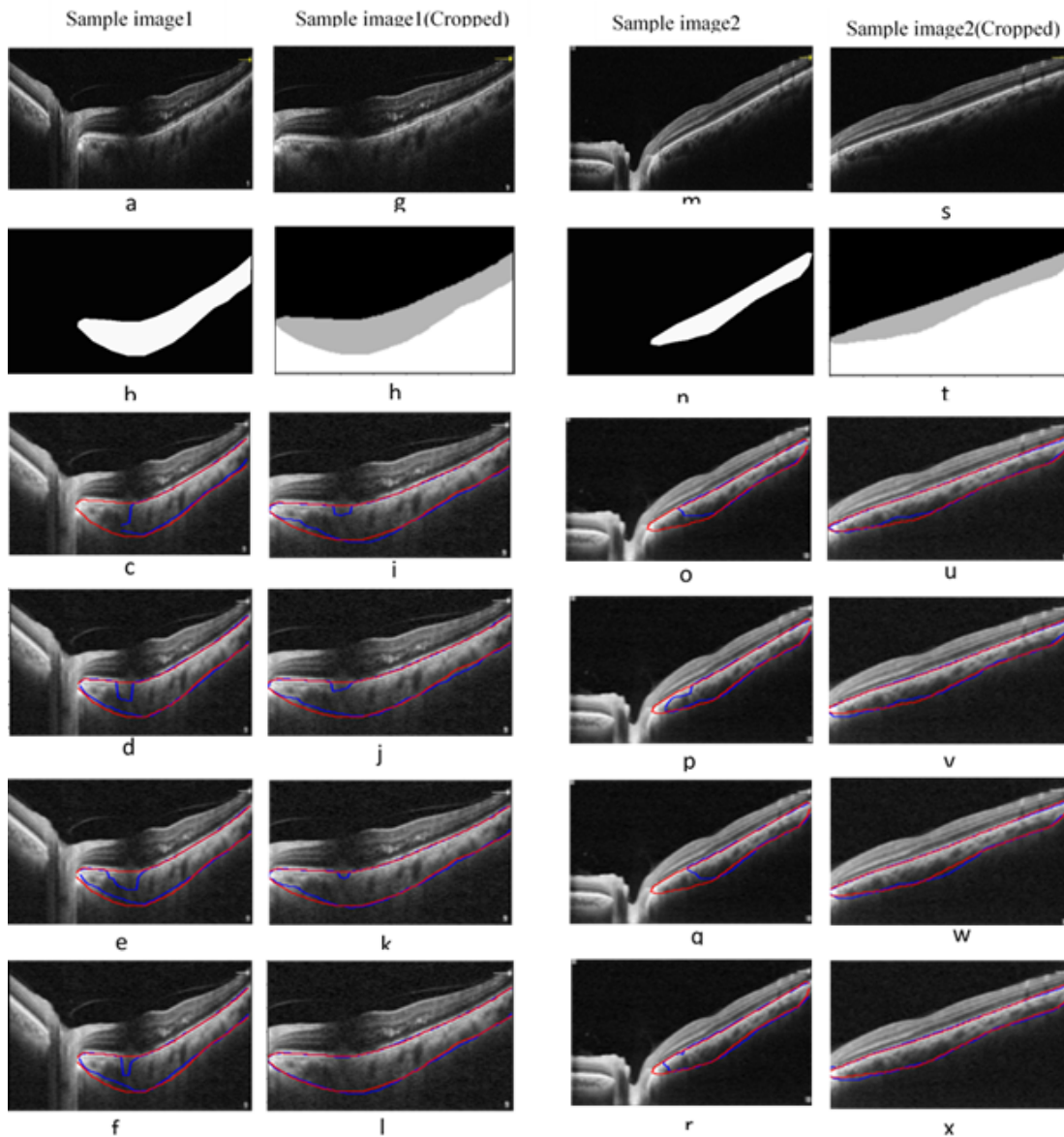


Figure 4

(a) Original diabetic retinopathy **subject 1**, (b) 2-class ground truth. Real and predicted boundaries of two-class using loss function: (c) DL, (d) DL +WCCE, (e) DL +WCCE + TV, (f) DL +WCCE + Tversky. (g) **Cropped original diabetic retinopathy subject 1**, (h) 3-class ground truth. Real and predicted boundaries of three-class using loss function: (i) DL, (j) DL +WCCE, (k) DL +WCCE + TV, (l) DL +WCCE + Tversky, (m). Original **diabetic retinopathy subject 2**, (n) 2-class ground truth. Real and predicted boundaries of two-class, using loss function: (o) DL, (p) DL +WCCE, (q) DL +WCCE + TV, (r) DL +WCCE + Tversky, (s) **Cropped original diabetic retinopathy subject 2**, (t) 3-class ground truth, real and predicted boundaries of three-class using loss function: (u) DL, (v) DL +WCCE, (w) DL +WCCE + TV, (x) DL +WCCE + Tversky. Manually annotated boundaries for each image are shown in red where predicted ones are shown in blue.

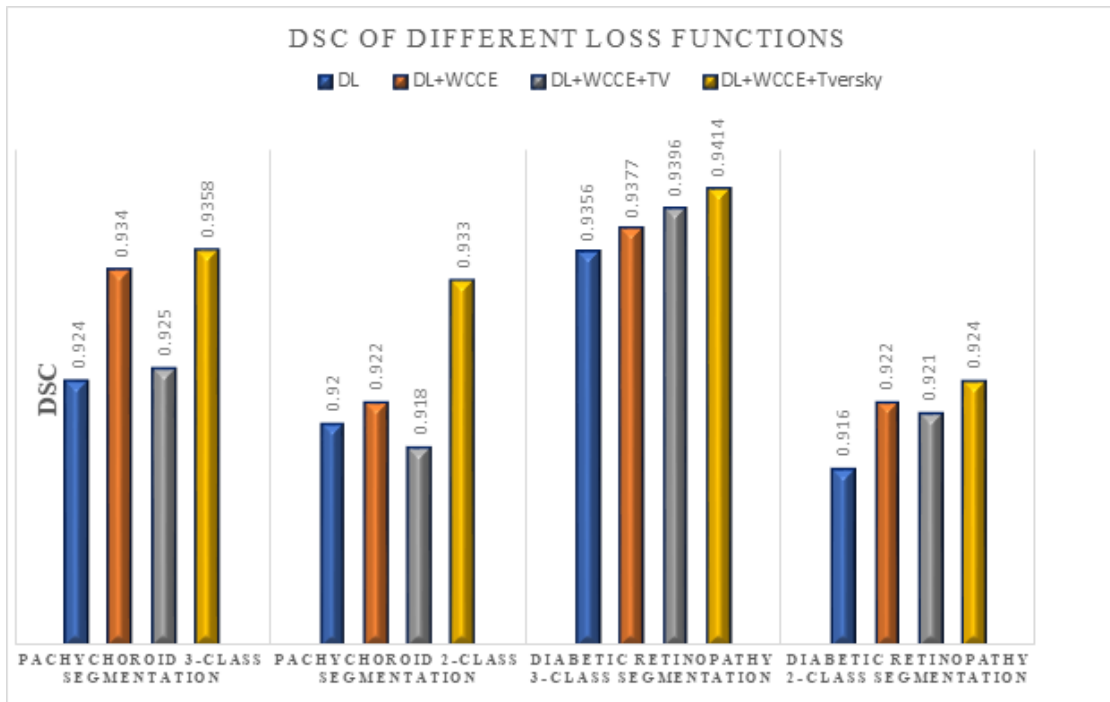


Figure 5

Comparison of DSC for different loss functions in pachychoroid spectrum and diabetic retinopathy datasets using 2 and 3-class segmentation

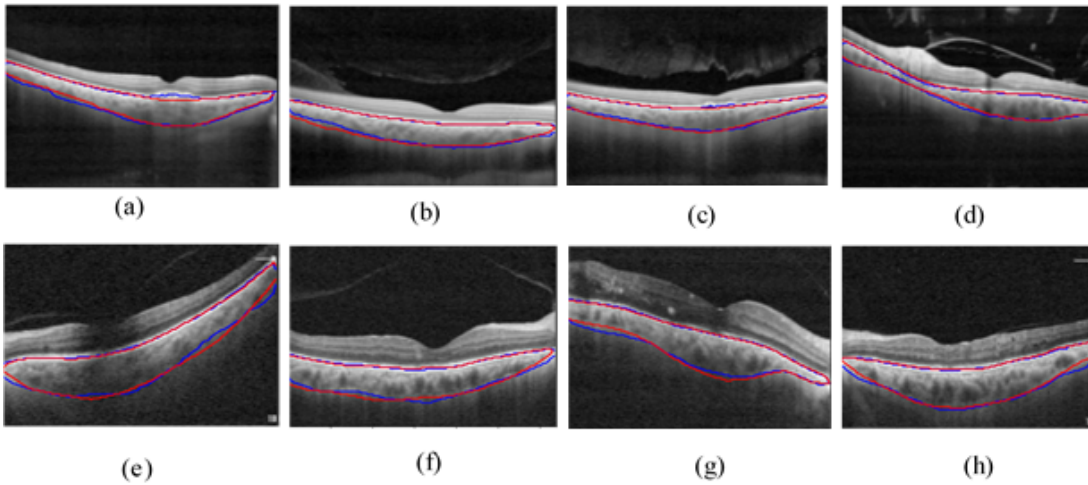


Figure 6

Illustrations of the four samples with final segmentation using the three-class approach with a combination of three loss functions (DL +WCC + Tversky). The first row belongs to the diabetic retinopathy dataset and the second row shows the results from pachychoroid spectrum dataset.

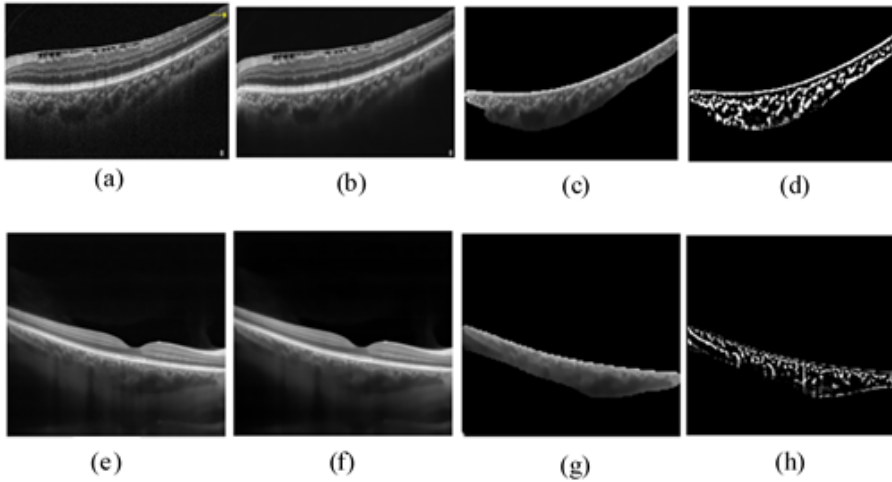


Figure 7

Illustration of the vascular LA detection using Niblack algorithm. First row: a) Original image (diabetic retinopathy). b) Denoised image c) Predicted choroid area, d) Vascular LA detection. Second row: e) Original image (pachychoroid spectrum). f) Denoised image, g) Predicted choroid area, h) Vascular LA detection.

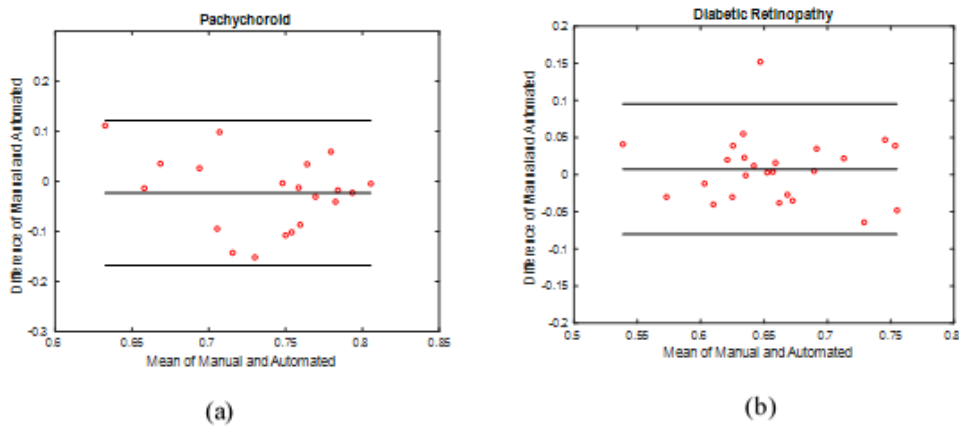


Figure 8

Bland Altman plot for manual and automated measurement of CVI in a) pachychoroid spectrum and b) diabetic retinopathy data.

Supplementary Files

This is a list of supplementary files associated with this preprint. Click to download.

- [Appendix.docx](#)